Three-Dimensional X-Ray Photoelectron Tomography on the Nanoscale: Limits of Data Processing by Principal Component Analysis

Hajati, Shaaker; Walton, J.; Tougaard, Sven Mosbæk

Published in:
Microscopy and Microanalysis

DOI:
10.1017/s1431927613000354

Publication date:
2013

Document version
Submitted manuscript

Citation for pulished version (APA):
Hajati, S., Walton, J., & Tougaard, S. (2013). Three-Dimensional X-Ray Photoelectron Tomography on the Nanoscale: Limits of Data Processing by Principal Component Analysis. Microscopy and Microanalysis, 19(3), 751-760. DOI: 10.1017/s1431927613000354

Microsc. Microanal. 19, 751–760, 2013
doi:10.1017/S1431927613000354

Microscopy AND Microanalysis

Three-Dimensional X-Ray Photoelectron Tomography on the Nanoscale: Limits of Data Processing by Principal Component Analysis

Shaaker Hajati,[1,*] John Walton,[2] and Sven Tougaard[3]

[1]*Department of Physics, Yasouj University, Yasouj 75918-74831, Iran*
[2]*School of Materials, The University of Manchester, Manchester M13 9PL, UK*
[3]*Department of Physics, Chemistry, and Pharmacy, University of Southern Denmark, DK-5230 Odense M, Denmark*

Abstract: In a previous article, we studied the influence of spectral noise on a new method for three-dimensional X-ray photoelectron spectroscopy (3D XPS) imaging, which is based on analysis of the XPS peak shape [Hajati, S., Tougaard, S., Walton, J. & Fairley, N. (2008). *Surf Sci* **602**, 3064–3070]. Here, we study in more detail the influence of noise reduction by principal component analysis (PCA) on 3D XPS images of carbon contamination of a patterned oxidized silicon sample and on 3D XPS images of Ag covered by a nanoscale patterned octadiene layer. PCA is very efficient for noise reduction, and using only the three most significant PCA factors to reconstruct the spectra restores essentially all physical information in both the intensity and shape of the XPS spectra. The corresponding signal-to-noise improvement was estimated to be equivalent to a reduction by a factor of 200 in the required data acquisition time. A small additional amount of information is obtained by using up to five PCA factors, but due to the increased noise level, this information can only be extracted if the intensity of the start and end points for each spectrum are obtained as averages over several energy points.

Key words: nondestructive analysis, 3D XPS imaging, XPS peak shape analysis, PCA noise reduction

Introduction

Interest in X-ray photoelectron spectroscopy (XPS) imaging has increased in the past decade due to both improvements in data acquisition and subsequent data processing. In particular, the application to determine accurate depth distributions on the nanometer scale is highly important. It is known that more information than that typically obtained from standard quantitative analysis, which relies on peak intensity, can be gained by an analysis that also includes the inelastic loss structure (i.e., XPS peak shape analysis) (Tougaard, 1996). XPS peak shape analysis gives the atomic percent of elements [or the number of atoms per unit surface area that we denote as the amount of substance (AOS)] in the outermost few nanometers, the depth distribution of atoms, and the surface concentration (Tougaard, 1996). However, XPS imaging still largely relies on peak intensities. Therefore, there is a need for improved methods to extract the maximum information available in the data.

Recently, images of film thickness, after noise reduction by principal component analysis (PCA), were obtained (Walton & Fairley, 2005) using ratios of peak area to background signal (Tougaard, 1987) for each pixel by angularly resolved XPS imaging (Artyushkova & Fulghum, 2005) and using XPS peak intensity (Smith et al., 2006; Payne et al., 2007). A method for quantitative XPS, which by analysis of both peak intensity and shape, automatically accounts for the effect of variation in atomic concentration with depth was developed by Tougaard and Hansen (1989) and by Tougaard (1990*a*, 1990*b*, 1996, 1998). Its validity was investigated (Hajati et al., 2007) through a series of systematic experiments, some of which were reviewed in Tougaard (1998), Hajati and Tougaard (2006, 2010), and López-Santos et al. (2010). The method relies on visual inspection of the agreement between the measured spectrum and a model spectrum, for different depth profiles over a wide energy range. Although it is quite accurate, and rather easy to apply, it requires operator interaction and is therefore not practical for XPS imaging where thousands of spectra must be analyzed.

Tougaard (2003) proposed a simplified algorithm to characterize the outermost three inelastic electron mean free paths (λ) of the sample. In this method, the background is adjusted to match the spectrum at just a single energy rather than over a wide energy range below the peak (Tougaard, 2003). This algorithm is of course less accurate than the previous, but it is well suited for automation. The validity was tested for large area ($\sim 5 \times 5$ mm^2) XPS taken from different nanostructures, and it was found that the AOS within the outermost 3λ ($AOS_{3\lambda}$) determined using this simplified method deviates less than 10% from the results obtained with other more elaborate techniques, and that surface, bulk, and homogeneous depth distributions can clearly be distinguished (Tougaard, 2005). For XPS imaging, each pixel is typically a few micrometers wide, and the signal intensity is orders of magnitude smaller compared to conventional XPS from a large surface area. For practical reasons, this cannot be compensated for by increas-

Received October 22, 2012; accepted January 30, 2013
*Corresponding author. E-mail: Hajati@mail.yu.ac.ir

ing the recording time because thousands of spectra must be recorded. The noise level is therefore typically orders of magnitude larger than in traditional XPS.

A qualitative test proved that in practice the algorithm could handle this rather well (Hajati et al., 2006). In that work, we applied a rule (Tougaard, 2003) to qualitatively categorize the pixels into three groups: those pixels where atoms are at depths $\leq 1\lambda$ (*surface*), at depths $\geq 1\lambda$ (*bulk*), and where atoms have a roughly constant concentration throughout the depth interval from 0 to 3λ (*homogeneous*), respectively. In another article (Hajati et al., 2008*a*), we also made a *quantitative* test of the algorithm by analyzing sets of Ag 3D XPS spectra taken from a series of samples with different effective thicknesses of plasma patterned octadiene (2, 4, 6, and 8 nm) on a silver substrate (Hajati et al., 2008*a*). We determined images of the amount of silver atoms in the outermost few nanometers of the samples. For a given sample, images of different sectioning of depth distributions of atoms were made, which clearly proved the potential of the method for quantitative, nondestructive imaging of the in-depth distribution of atoms, as well as of the $AOS_{3\lambda}$ in the outermost few nanometers, and therefore the ability to produce 3D images. In Hajati et al. (2006, 2008*a*), we applied the algorithm to relatively strong XPS peaks, and the data acquisition time was also rather long. The spectra were smoothed using a quadratic, 7-point Savitzky-Golay filtering (Savitzky & Golay, 1964) followed by pixel averaging. However, this procedure for noise reduction may not be sufficient for imaging of atoms with a small ionization cross section. Furthermore, it would be a significant advantage for practical use if the data acquisition time could be reduced, which however would lead to increased noise. Therefore, more efficient methods for noise reduction such as PCA, which utilizes the full set of data, may be expected to give further improvement in the signal-to-noise ratio (SNR).

The potential for noise reduction in XPS using PCA has been well documented (Malinowski & Howery, 1980; Geladi & Grahn, 1996; Jolliffe, 2002; Briggs & Grant, 2003; Walton & Fairley, 2005; Hajati et al., 2008*b*). PCA assumes that any dataset can be described by a linear combination of one or more pure components. By multiplying the data matrix by its transpose, a covariance matrix is formed that can then be decomposed into an orthogonal dataset, using the singular value decomposition procedure (Walton & Fairley, 2005), from which the maximum variation in the data is partitioned into abstract components with the largest eigenvalues. The abstract factors without features can be attributed to noise. If the original dataset is reconstructed from only those abstract factors containing significant information, the result is a new dataset where the contribution from noise is reduced in magnitude. PCA can be applied to the data as a set of images incremented in energy, or as a set of spectra from a given spatial location. However, the size of the covariance matrix is dependent on the route chosen. For a dataset consisting of images of 256 pixels × 256 pixels and 114 energy steps, the covariance matrix constructed from the images would have dimensions of 114 × 114, while the covariance matrix constructed from the spectra would have dimensions of 65,536 × 65,536. Clearly, the computational requirements for decomposition of the covariance matrix using a standard procedure would be prohibitive in the latter case, although partitioning the information content into a large number of factors is advantageous because it enables superior separation of information from the noise in the dataset (Browning, 1993).

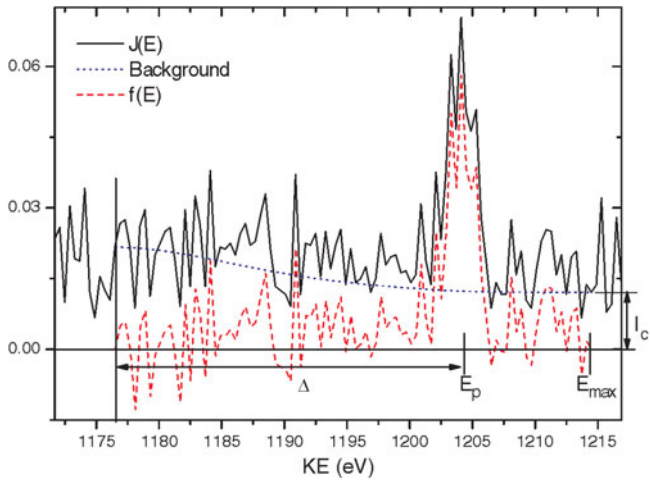

Figure 1. Definition of quantities used in the Materials and Methods section (a typical C 1s spectrum).

In Hajati et al. (2008*a*), we investigated the capability of this new method for 3D XPS imaging using simpler methods rather than the PCA method for noise reduction. In Hajati et al. (2008*b*), we studied the effect of PCA noise reduction on 3D images of carbon and oxygen of a patterned oxidized silicon sample, and it was found to be very effective.

In imaging, data acquisition time is a limiting factor, which can be reduced by effective and optimized noise reduction procedures. It is clear that when the spectra are reconstructed from abstract factors, using fewer factors gives larger noise reduction and therefore sharper images. However, using fewer factors also reduces the physical information in the reconstructed spectra. In this article, we therefore investigate the influence of the number of factors used on image quality and accuracy. To this end, we study in detail the influence of PCA on 3D XPS images of Ag covered by a nanoscale patterned octadiene and on 3D images of carbon contamination of patterned oxidized silicon.

Materials and Methods

In this section, we summarize the algorithm derived in Tougaard (2003). Let $J(E)$ denote the energy distribution of emitted electrons. The peak structure of interest is centered around the energy E_p, and the high energy end of the spectrum E_{max} is chosen a few eV (about 5–10 eV) above the peak structure (see Fig. 1). All energies are given in kinetic energy.

For analysis of C 1s, we use the three-parameter universal cross section (Tougaard, 1997) with parameters $C = 750$

Table 1. Rules to Estimate the Depth Profile from L^* (Tougaard, 2003, 2005) (see section III.B in Tougaard, 2005 for experimental proof of the rules).

	L^*	Depth Distribution
Rule I:	$0 < L^* \lesssim 1$	Most atoms are at depths $< \lambda$ (surface region)
	$-1 \lesssim L^* < 0$	Most atoms are at depths $> \lambda$ (bulk region)
	$2 \lesssim \lvert L^* \rvert$	Approximately constant (homogeneous region)
If the same peak from two samples, in this case two pixels, have values L_1^* and L_2^*, then		
Rule II:	$0 < L_1^* < L_2^* \lesssim 1$	Atoms are surface localized in both samples, and the atoms are at more shallow depth in sample 1 than in sample 2.
Rule III:	$L_1^* < L_2^* < 0$	Atoms are primarily in the bulk of both samples and at deeper depth in sample 2 than in sample 1.

and $D = 436$ eV^2. For Ag 3d, we use the two-parameter universal cross section (Tougaard, 1997) with parameter $C = 1643$ eV^2. The first step in the peak shape analysis is to correct for inelastic electron scattering and to calculate the background-subtracted spectrum, $f(E)$ [see equation (12) in Tougaard, 2003 for details of the algorithm].

$$f(E) = J(E) - B_1 \int_E^{E_{\max}} J(E') \times \frac{E' - E}{[C - (E' - E)^2]^2 + D(E' - E)^2}\, dE' \qquad (1a)$$

for C 1s and

$$f(E) = J(E) - B_1 \int_E^{E_{\max}} J(E') \frac{E' - E}{[C + (E' - E)^2]^2}\, dE' \qquad (1b)$$

for Ag 3d, for the energy range $E_p - \Delta < E < E_{\max}$, where Δ is chosen between 20 and 40 eV (see Fig. 1). It has been shown that the result of the analysis does not depend significantly on the exact value of Δ as long as it is in this range (Tougaard, 2005). Here we have used $\Delta = 30$ eV. B_1 is adjusted such that $f(E_p - \Delta) = 0$.

From $f(E)$, the peak area is determined

$$A_p = \int_{E_p - \Delta}^{E_{\max}} f(E)\, dE. \qquad (2)$$

To make an absolute determination of the AOS, it is necessary to calibrate the instrument. This may be done by analysis of the spectrum for the same XPS peak from a solid with homogeneous distribution of atoms of density c_H. Let B_0 and A_p^H denote the B_1 and A_p values obtained from analysis by equations (1) and (2), respectively, of the spectrum from the homogeneous reference.

Now calculate (Tougaard, 2003)

$$L^* = L/3\lambda = \frac{B_1}{B_0 - B_1} (\cos\theta)/3, \qquad (3)$$

where θ is the angle of emission with respect to the surface normal. Note that in the algorithm (Tougaard, 2003) all kinds of depth distributions are approximated by an exponentially varying function with decay constant $1/L$. This means that the value of L and therefore the value of L^* give a rough indication of the in-depth distribution of atoms. In practice, it has been found that the rules in Table 1 apply (Tougaard, 2003, 2005, 2013).

Furthermore, the amount of substance within the outermost 3λ is (Tougaard, 2003)

$$AOS^* = 100 \times \frac{L^* + (\cos\theta)/3}{1 - e^{-[(3/\cos\theta) + (1/L^*)]}} (1 - e^{-1/L^*}) \frac{A_p}{A_p^H}, \qquad (4)$$

where we have set $c_H = 1$ and consequently AOS^* is the amount of atoms within depths 3λ relative to the amount of atoms in the same volume of the reference sample.

For the present analysis, we use the C1s spectra from Hajati et al. (2008*b*) and the Ag3d spectra from Hajati et al. (2008*a*) and give in the following two subsections a brief summary of the origin of the spectra.

Carbon Contamination on Thermally Oxidized Silicon Patterned Structure

A silicon wafer was thermally oxidized using dry oxidation at about 1050°C and then etched to produce a patterned structure (for details see Hajati et al., 2008*b*). All data were acquired on a Kratos Axis Ultra (Kratos Analytical, Manchester, UK) utilizing a delay line detector for pulse counting electrons (for details see Hajati et al., 2008*b*). Spectrum image datasets of 256×256 pixels were acquired from an area of $800\ \mu\text{m} \times 800\ \mu\text{m}$.

Spectra saved in the VAMAS (Dench et al., 1988) format were converted to QUASES format using a FORTRAN code that we made for this purpose. Reference C 1s spectra were taken from highly oriented pyrolytic graphite (HOPG) cleaved prior to insertion into the instrument. The images were converted into a spectrum at every pixel and summed to produce the C1s reference spectrum.

Silver Covered by Plasma Decomposed Patterned Nanoscale Octadiene Layer

A grid with a 125 μm opening was placed over the silver substrates. The sample was produced by exposing this to a plasma created by radio-frequency dissociation of octadiene (d'Agostino, 1990; Alexander et al., 2004). The sample thickness was estimated from a calibration made in a previous set of experiments of discharge time versus thickness determined with a Jobin Yvon ellipsometer (Horiba Jobin Yvon,

Longjumeau, France). The resulting sample consists of an Ag substrate with strip-like patterned overlayer having nominal thicknesses of ~6 nm (for details see Hajati et al., 2008*a*).

The XPS data were acquired on a Kratos Axis Ultra X-ray photoelectron spectrometer fitted with a delay line detector (Walton & Fairley, 2006) using monochromatic Al Kα radiation (for details see Hajati et al., 2008*a*). Parallel XPS image datasets of 256 × 256 pixels, from an area of 400 μm × 400 μm, were acquired from the patterned polymer. Spectra saved in VAMAS format were converted to QUASES format. A spectrum taken from a pure Ag sample was used as reference.

Results

We used CasaXPS (Fairley, 2008) for PCA data processing. To facilitate further data processing, the image datasets were reduced in size to 128 × 128 pixels by averaging the spectra taken from every four pixels. Using PCA processing as described above, the spectra were decomposed into their principal components, which here are referred to as image abstract factors. The proposed data treatment based on the background analysis was chosen instead of just peak area ratio (C1s/O1s or C1s/Si2p for example 2A; C1s/Ag3d for example 2B) because the latter method applies only for cases in which the overlayer is uniform and covers the complete analyzed surface. Therefore, the approach based on the peak area ratio is mostly useful for obtaining thicknesses of overlayers and does not provide the distribution of chemical phases in the 3D volume of the material.

Results and Discussion for the Analysis of C 1s

This analysis involved looking at the C1s signal from carbon contamination on a thermally oxidized silicon patterned structure. Figure 2a shows the C1s spectrum from a given pixel, and Figure 3 shows the five image abstract factors for C1s with the largest eigenvalues, which are shown in Figure 4. Several datasets were reconstructed using the first 2, 3, 4, 5, and 6 image abstract factors, respectively, for the C 1s datasets. The images corresponding to each pixel were then converted to a spectrum. The reconstructed spectra obtained after using the first 2, 3, 4, 5, and 6 principal components are shown in Figure 2b for the same pixel shown in Figure 2a. Note the substantial decrease in noise level between the raw spectrum in Figure 2a and the reconstructed spectrum in Figure 2b. Note also that the reconstructed spectrum using 2 factors has a significantly lower noise level than the spectrum obtained with 6 factors.

We can estimate the benefit of this PCA data processing on the SNR from the C1s spectrum in Figure 2. The noise reduction is a factor of ~50, 15, and 4 using 2, 3, and 6 factors, respectively. The corresponding time reduction would then be (assuming the SNR to be proportional to the square root of the measuring time) 2500, 225, and 16, respectively. In the shown examples in the present article, the total data acquisition time was ~3 h. It is therefore clear that it is important to find the minimum number of factors that will still contain essentially all the physical information in the spectra.

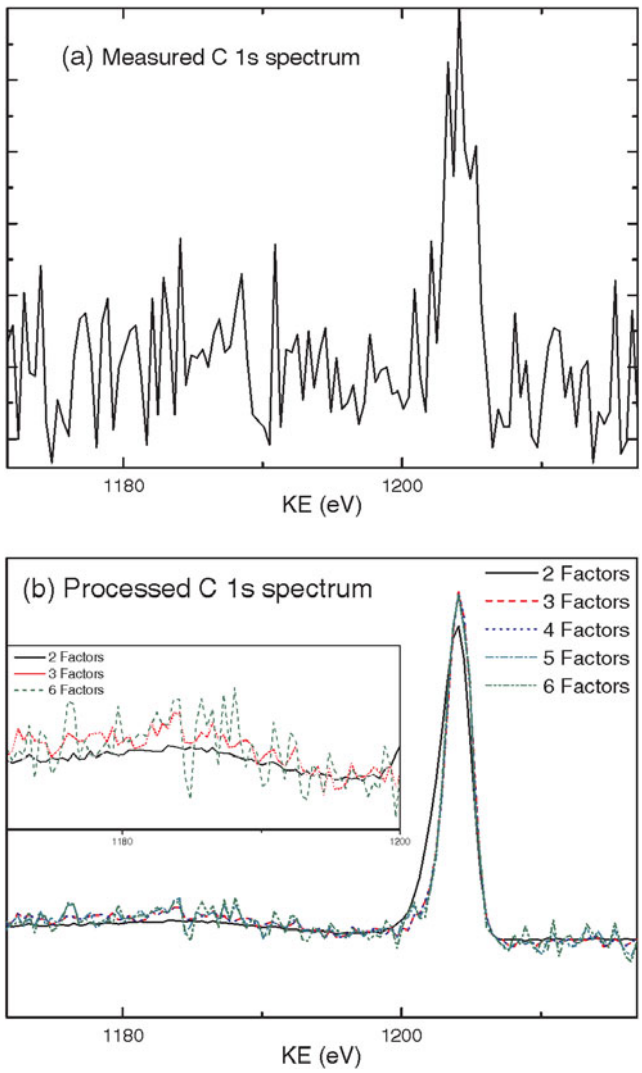

Figure 2. C1s spectrum for a given pixel: (**a**) measured and (**b**) after PCA processing using a different number of factors.

In this article, we want to investigate to what extent different noise reduction procedures can improve the obtained quantitative images. To this end, we have made different datasets using different data processing namely: (1) raw data without any further processing and (2) spectra using 2, 3, 4, 5, and 6 factors as described above. The images were produced by applying the algorithm outlined above. To determine the intensity at the energies $E_p - \Delta$ and E_{max}, averaging over six energy points was done. Now, a constant intensity I_c equal to that at energy E_{max} (Fig. 1) was subtracted from the entire spectrum, and the spectra were automatically analyzed using a PC program implementing the algorithm (Tougaard, 2003) as outlined above to produce several images.

In the present analysis, we used $\Delta = 30$ eV and $\lambda = 3.3$ nm at 1200 eV (corresponding to the C 1s peak) as estimated using the TPP-2M formula (Tanuma et al., 1994).

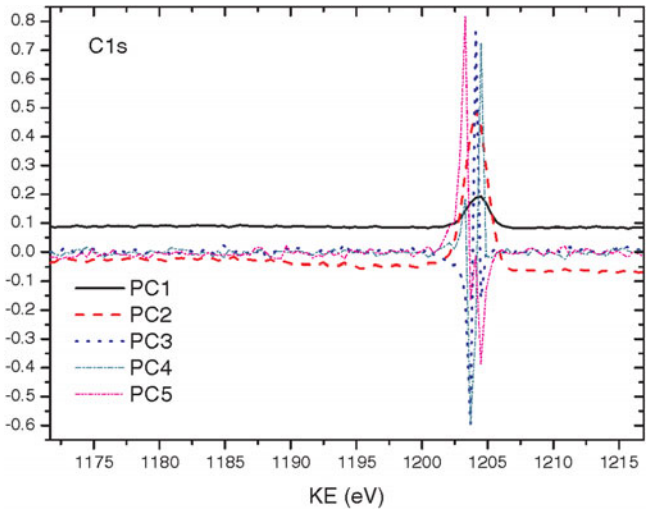

Figure 3. First 5 principal components for C 1s.

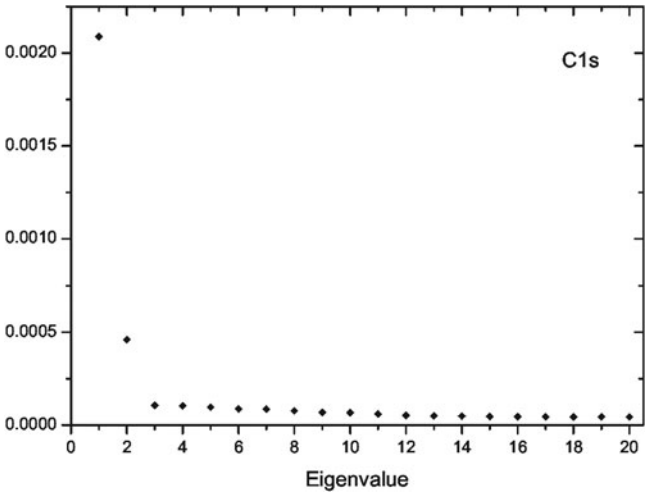

Figure 4. First 20 largest eigenvalues for C 1s.

Finally, applying equations (1a) and (2) to analyze the C 1s reference spectrum of HOPG, the values $B_0 = 504$ eV^2 and $A_p^H = 0.367$ eV were obtained. In the same way, B_1 and A_p were obtained for each pixel for C1s. Inserting the B_1 values in equation (3), we obtain L^* from which the depth profile information (see Figs. 5–10) is obtained according to the rules in Table 1. Using equation (4), we now calculate the AOS^* for each pixel for carbon (Fig. 11). For example, $AOS^* = 0.25$ in a given pixel means that the AOS (within depths $3\lambda = 9.9$ nm) is 25% of that for HOPG.

Images of L^* and AOS^* for carbon contamination collected using the above-mentioned procedures are shown in Figures 5–10 and 11, respectively. Using the raw data (as measured), the AOS^* image shows no features (Fig. 11f). Images of the depth distributions corresponding to the different ranges of L^* values are shown in Figures 10a–10e. Note that larger L^* means thicker carbon layer (Table 1). The results of PCA illustrated in rows a–e in Figures 5–9 show increasing positive L^* values, which according to rule II in Table 1 corresponds to images of the surface that have increasingly larger overlayers of carbon. A rough calibration of the correspondence between L^* and the depth scale was made in the following way: For instance, as seen in Figure 6, for most pixels, L^* has positive value from ~0.07 (Fig. 6a) to ~0.55 (Fig. 6d). According to rule I in Table 1, this means that the thickness of carbon contamination is not larger than $\sim 1\lambda$ (3.3 nm). According to rule II in Table 1, thickness increases in Figures 6a–6e as the L^* values increases. On the other hand, the pixels (black) shown in Figure 6a with L^* values about ~0.07, from Figure 11b, can be seen to have their corresponding AOS^* not larger than 0.06. $AOS^* = 1$ means that the layer thickness is 3λ (~9.9 nm) and $AOS^* = 0.06$ therefore corresponds to ~0.5 nm. In other words, $L^* = \sim 0.07$ corresponds to ~ 0.5 nm. This procedure was used to make a rough calibration of the depth scale corresponding to the different ranges of L^* values, and the gradual increasing thickness of C contaminations from 0 to 3 nm is shown in the far left column of Figures 5–10.

As seen in Figures 5–10 and in Figure 11, a clear improvement is obtained due to PCA processing. In particular, using only 2 factors gives a very sharp image in both the depth profile images in Figure 5 and the AOS^* images in Figure 11a. The images with more factors are less sharp, although even with 6 factors, it is substantially sharper than the unprocessed data which show no structure. The question is how many factors are needed to make sure that the images contain all essential physical information. In the patched areas, which correspond to the regions of the SiO_2 surface that were etched, the carbon thickness is ~0.5 nm, whereas it is thicker for most pixels outside of these regions. In a region in the upper left corner of the images, there is a carbon contamination layer that is substantially thicker as clearly seen in Figures 6c and 6d (obtained with 3 factors). On the other hand, this area is, in Figure 5 (obtained with 2 factors), seen as a thinner layer because the region is present in Figure 5b but not in Figure 5c. This illustrates that with 2 factors some information has been lost and that 3 factors are needed to resolve the true thickness of the carbon layer in this region.

The origin of this is clear from Figure 3, which shows that the second factor (PC2) has negative intensity except in the peak region. This affects the spectrum and lowers its background (Fig. 2b), which in turn affects the resulting thickness and gives a thinner layer. Increasing the number of factors gives a noisier signal, but the background of the signal gets closer to the true one (Fig. 2b), and consequently this gives more reliable images. There are only small differences between the images for 3, 4, and 5 factors. Therefore, images obtained with any of the number of factors 3, 4, 5, or 6 give practically equally sharp and accurate images and can be used for data processing, but with 2 factors the images are significantly different. However, there are small differences between the images obtained with 3, 4, and 5 factors. That there is a small additional information in factors 4 and 5 is also consistent with the fact that although the eigenvalues for factors 3, 4, and 5 are very small, they are slightly larger than for the higher order factors.

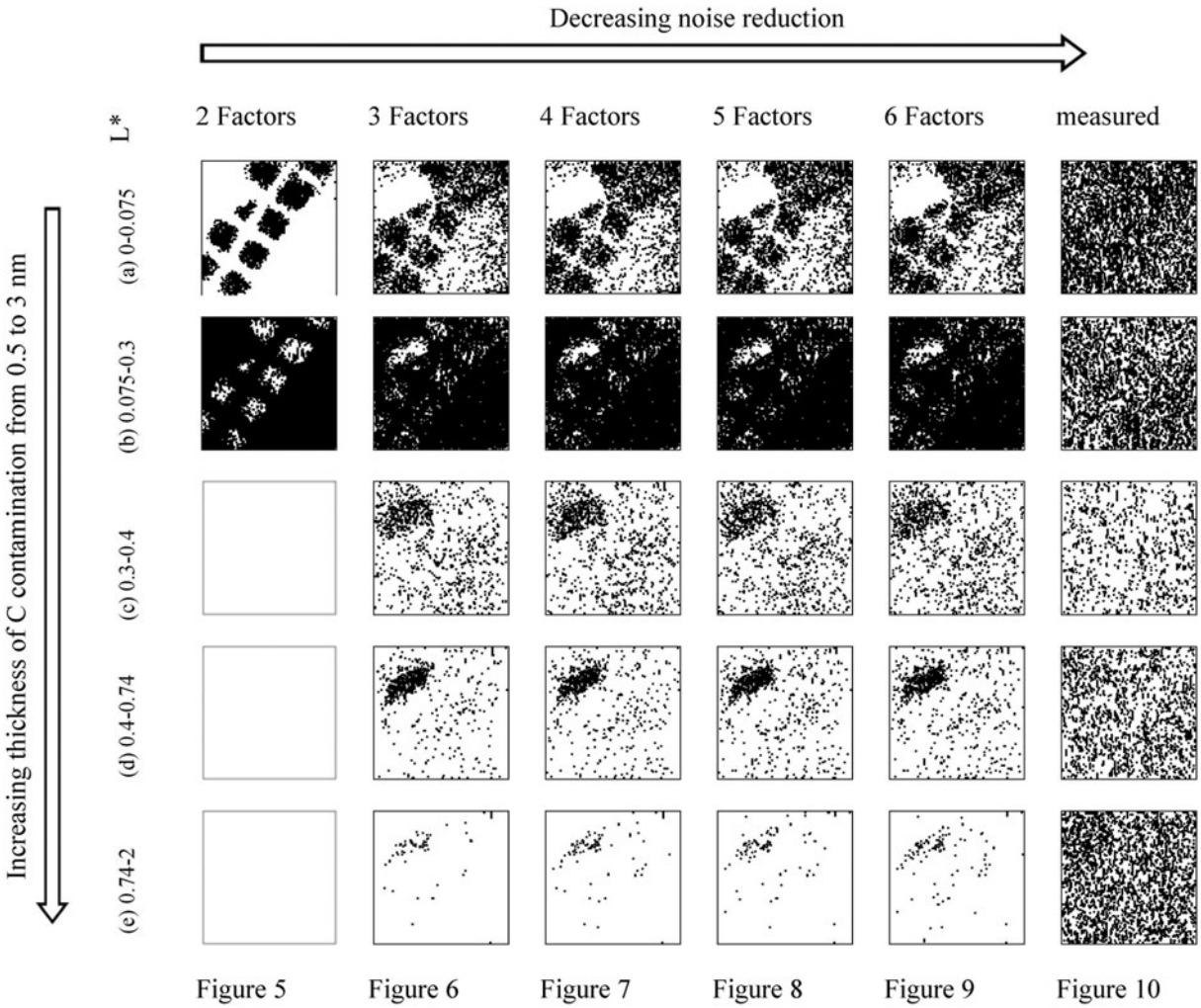

Figures 5–10. Images of carbon contamination. Note that black for a given pixel indicates that L^* is in the specified range. Arrow direction shows the increase in thickness of *C* contamination.

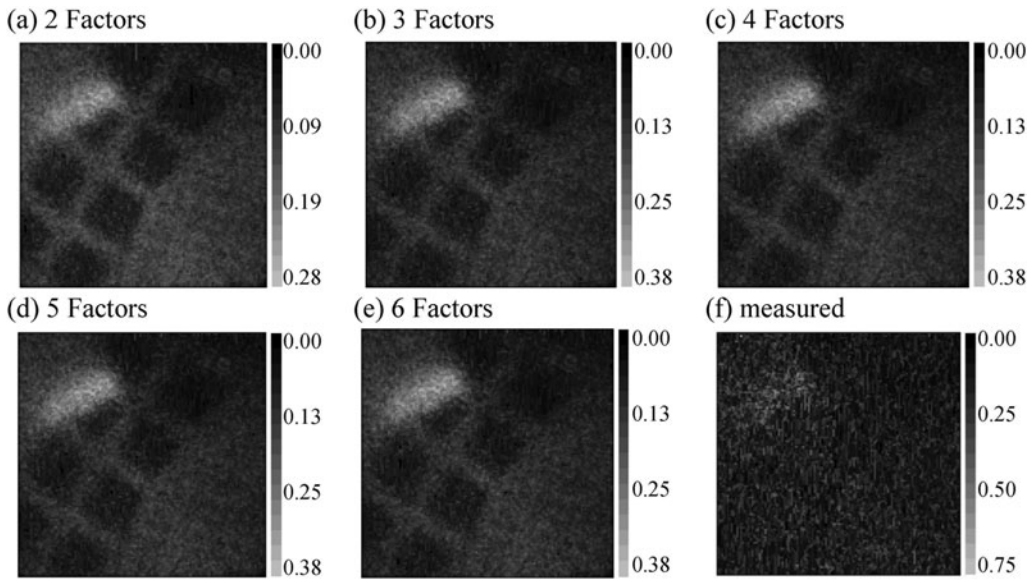

Figure 11. Images of AOS^* of carbon contamination.

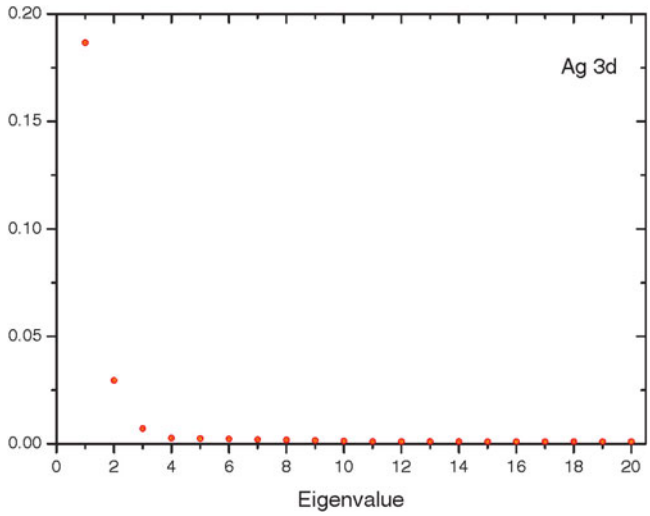

Figure 12. First 20 largest eigenvalues for Ag 3d.

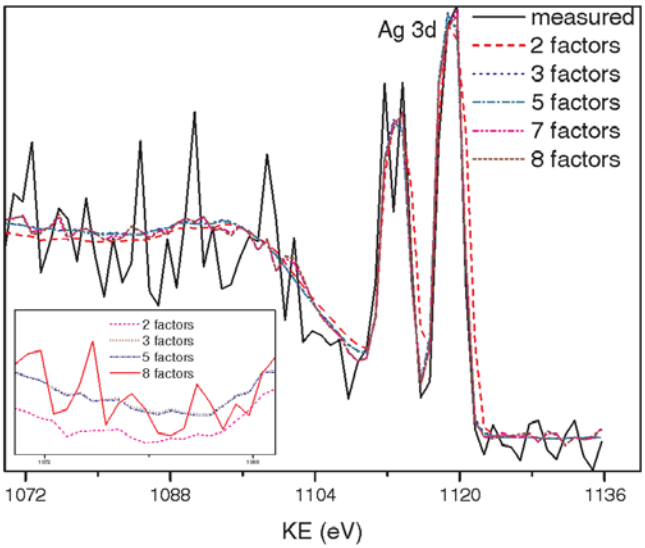

Figure 13. Ag 3d spectrum for a given pixel before and after PCA processing using a different number of factors. The background of the signal after 2 factors is *lower* than others for this pixel.

Using 5 factors gives more noisy spectra than using 3 factors (see inset in Fig. 2b). In spite of this, the noise in the obtained images is similar because to determine the intensity at the energies $E_p - \Delta$ and $E_{\max}$, averaging over six energy points was done.

Results for the Analysis of Ag 3d

This analysis was made looking at the Ag3d signal from the silver substrate. The Ag3d spectra were processed in a similar way as the C1s spectra. The eigenvalues for the 20 largest factors are shown in Figure 12. Several datasets were reconstructed using the first 2, 3, 5, 7, and 8 image abstract factors, respectively, for the Ag 3d datasets. The Ag 3d spectra measured for two pixels on the surface are shown in Figures 13 and 14. Also shown are the reconstructed spectra using the first 2, 3, 5, 7, and 8 principal components for the same two pixels. Calculations for determination of the

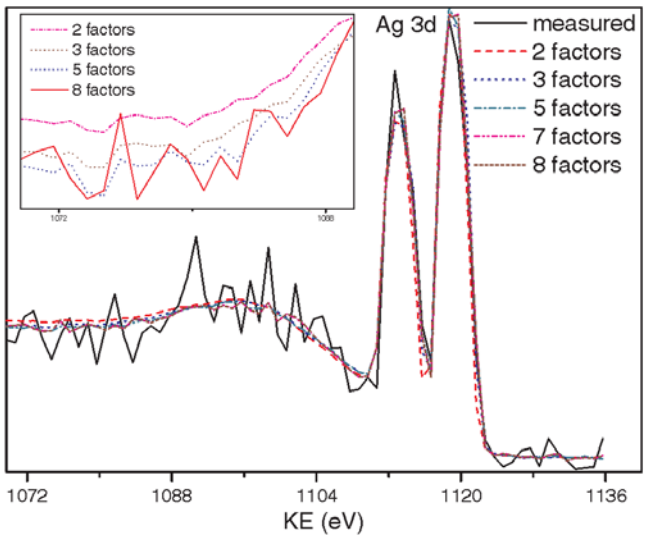

Figure 14. Ag 3d spectrum for a given pixel before and after PCA processing using a different number of factors. The background of the signal after 2 factors is *higher* than others for this pixel.

images of AOS^* and L^* for Ag 3d were done in a similar way as for carbon contamination on the other sample (see above). The Ag 3d signal is much larger than the C1s signal, and therefore contrast in the images, which reflects the sample depth composition, can be seen even for the unprocessed data in Figures 15f and 21. However, there is a clear change in sharpness of the images with PCA noise reduction. For most pixels, L^* is negative, which, according to the rules in Table 1, shows that the Ag atoms are covered by the octadiene overlayer. As seen in Figure 13, the background of the signal using 2 factors is lower than when using more than 2 factors for this pixel. A smaller background intensity corresponds to a thinner octadiene layer. On the other hand, for the pixel in Figure 14, the background of the signal using 2 factors is higher than the rest. Therefore, with only 2 factors, the analysis gives a thicker octadiene layer on top of the Ag substrate for this pixel. This means that although with 2 factors the images are very sharp, the depth information in the images is not accurate. Comparing row a in Figures 16–21, we see that for 3, 5, and 7 factors there are no pixels corresponding to this level of overlayer thickness. Using 2 factors there are some pixels in row a. For the image obtained with the unprocessed and with 8 factors, there are also pixels corresponding to this range of L^* values. We interpret this as being due to overprocessing of the data with 2 factors and increased influence of noise for 8 factors and for the unprocessed data, respectively. Similar effects can be seen when comparing the spectra for the other rows. From the inset of Figures 13 and 14, it is also seen that the background of the signal using 3, 5, 7, and 8 factors are fairly similar for each of the two pixels but significantly different than that of the signal using 2 factors. The signals with 7 and 8 factors have higher noise level than that for 2, 3, and 5 factors. In addition, the background of each of the signals after 3, 5, 7, and 8 factors is closer to the true one (see Figs. 13, 14). It is also seen that using either 3 or 8

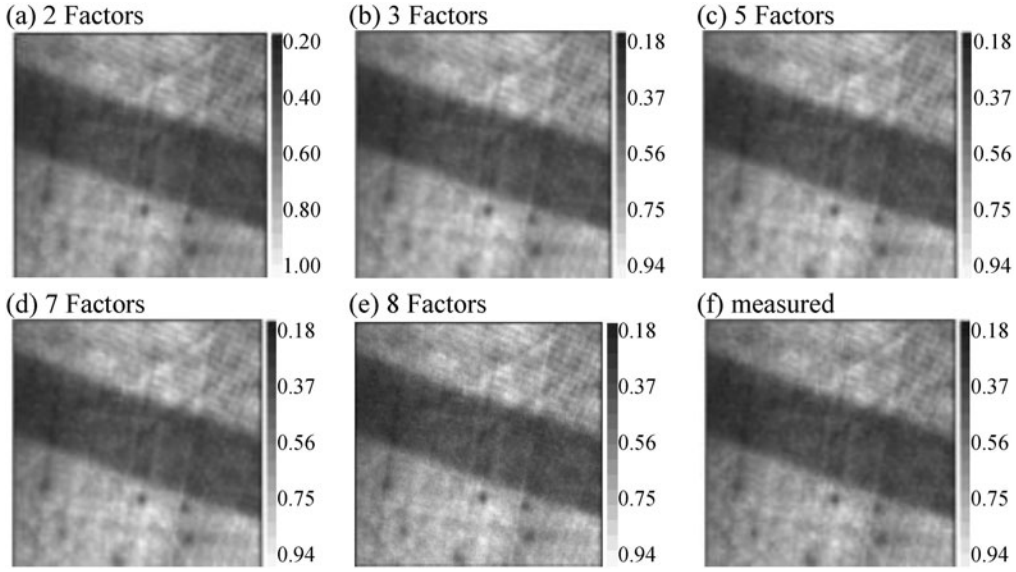

Figure 15. Images of AOS^* of Ag.

factors gives very good contrast for the images of depth distribution of atoms (rows a–h in Figs. 17, 20). This is also consistent with Figure 12, which shows that the eigenvalue for factor 3 is larger than that for the higher order factors. We therefore conclude that images obtained using at least 3 factors are reliable and accurate. Eigenvalues for factors 4 and 5 are clearly smaller than for factor 3, but they are still slightly larger than for the higher order factors. This indicates that the very small differences seen between the images using 3 and 5 factors in Figures 17 and 18 are real. Images obtained using 4 and 6 factors (not shown here) were very similar to those obtained using 5 factors.

In the applied algorithm (Tougaard, 2003), accuracy of the intensity I_c at $E_{\max}$ and the intensity at energy $E_p - \Delta$ are crucial. It should be noted that to determine these intensities, averaging over six energy points was done for both the C1s and Ag3d analysis. Therefore, although the noise level increases with the number of factors, the effect of this on these two numbers is small. Without using this procedure, there would be higher noise levels in the images (in particular for the C1s images) when more than 3 factors are used in the PCA procedure because this increases the noise level in the background in Figures 2b, 12, and 14.

Conclusion

We have studied in detail the influence of noise reduction by PCA on 3D XPS images of carbon contamination of a patterned oxidized silicon and on 3D XPS images of Ag covered by a nanoscale patterned octadiene. This investigation is important because, in imaging, data acquisition time is a limiting factor, which potentially can be reduced by effective and optimized noise reduction procedures. Thus, when a smaller number of PCA components are used to reconstruct the spectra, the noise level decreases but, at the same time, the spectra will be less accurate. It was found that essentially all physical information in the intensity and shape of the spectra is restored using only the three most important PCA factors. The corresponding signal-to-noise improvement was estimated to be equivalent to a reduction by a factor of 200 in the required data acquisition time. A small additional amount of information is obtained using up to 5 factors, but due to the increased noise level, this information can only be extracted if the intensity of the start and end points for each spectrum are obtained as averages over several points.

Acknowledgments

The authors thank Sarah Coultas (Kratos Analytical, Manchester, UK) for taking the Ag spectra. Financial support from The Danish Research Council for Independent Research–Natural Sciences is acknowledged.

References

Alexander, M.R., Wittle, J.D., Barton, D. & Short, R.D. (2004). Plasma polymer chemical gradients for evaluation of surface reactivity: Epoxide reaction with carboxylic acid surface groups. *J Mater Chem* **14**, 408–412.

Artyushkova, K. & Fulghum, J.E. (2005). Angle resolved imaging of polymer blend systems: From images to a 3D volume of material morphology. *J Electron Spectrosc Relat Phenom* **149**, 51–60.

Briggs, D. & Grant, J.T. (2003). *Surface Analysis by Auger and Photoelectron Spectroscopy*. Chichester, UK: IM Publications.

Browning, R. (1993). Multi-spectral imaging in materials microanalysis. *Surf Interface Anal* **20**, 495–502.

d'Agostino, R. (1990). *Plasma Deposition, Treatment, and Etching of Polymers*. London: Academic Press.

Dench, W.A., Hazell, L.B. & Seah, M.P. (1988). VAMAS surface chemical analysis standard data transfer format with skeleton decoding programs. *Surf Interface Anal* **13**, 63–122.

Fairley, N. (2008). CasaXPS Version 2.3.14: Software package for data processing. Available at http://www.casaxps.com.

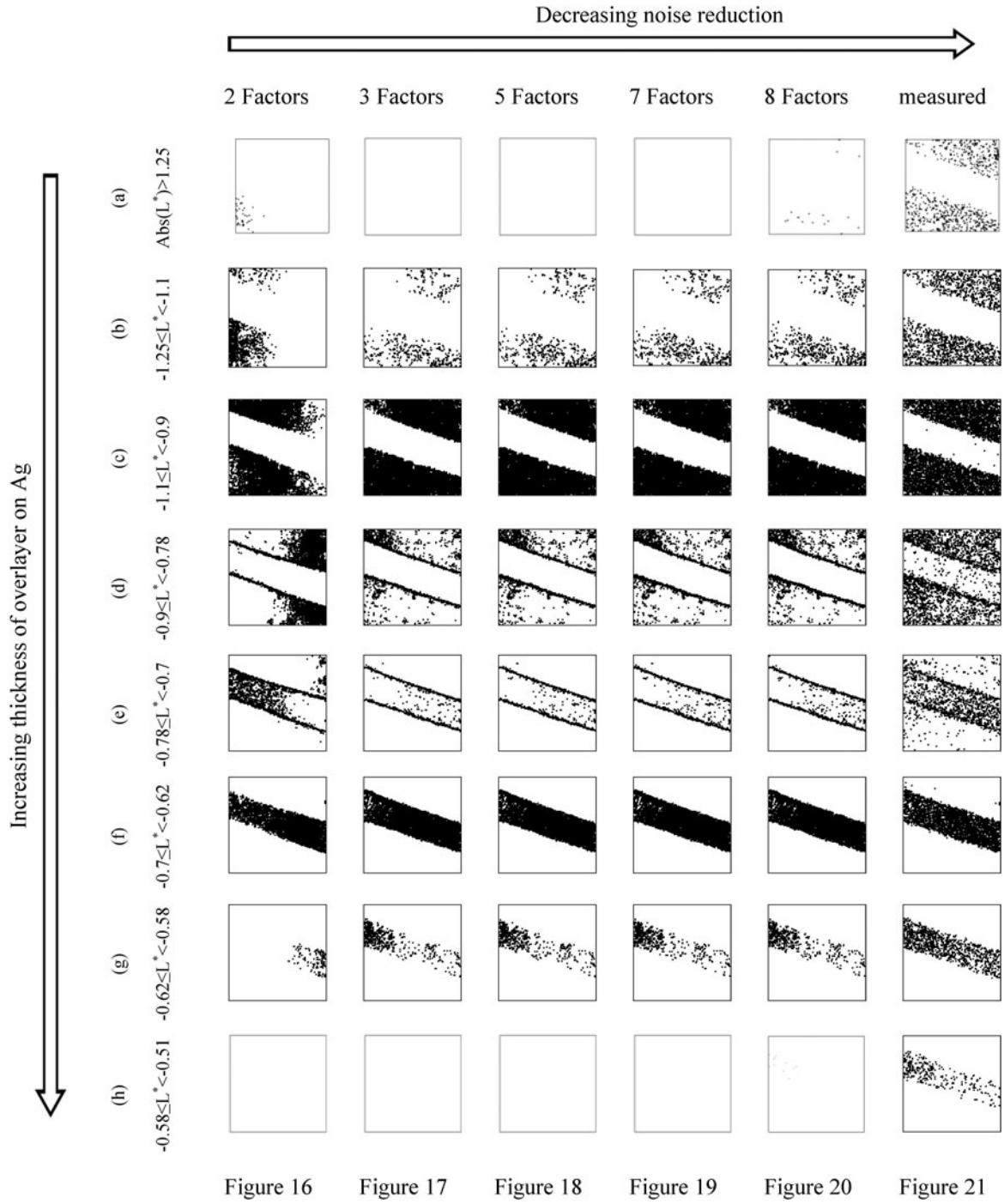

Figures 16–21. Images of L^* of Ag. Note that black or gray for a given pixel indicates that L^* is in the specified range. Arrow direction shows the increase in thickness of the over layer under in which the Ag is buried.

Geladi, P. & Grahn, H. (1996). *Multivariate Image Analysis*. Chichester, UK: Wiley.

Hajati, S., Coultas, S., Blomfield, C. & Tougaard, S. (2006). XPS imaging of depth profiles and amount of substance based on Tougaard's algorithm. *Surf Sci* **600**, 3015–3021.

Hajati, S., Coultas, S., Blomfield, C. & Tougaard, S. (2008*a*). Nondestructive quantitative XPS imaging of depth distribution of atoms on the nanoscale. *Surf Interface Anal* **40**, 688–691.

Hajati, S. & Tougaard, S. (2006). What nano-physical properties can be determined by analysis of elastic peak accompanied by its inelastic background tail in XPS and AES spectra? *J Surf Anal* **13**, 148–155.

Hajati, S. & Tougaard, S. (2010). XPS for non-destructive depth profiling and 3D imaging of surface nanostructures. *Anal Bioanal Chem* **396**, 2741–2755.

Hajati, S., Tougaard, S., Walton, J. & Fairley, N. (2008*b*). Noise reduction procedures applied to XPS imaging of depth distribution of atoms on the nanoscale. *Surf Sci* **602**, 3064–3070.

Hajati, S., Zaporojtchenko, V., Faupel, F. & Tougaard, S. (2007). Characterization of Au nano-cluster formation on and

diffusion in polystyrene using XPS peak shape analysis. *Surf Sci* **601**, 3261–3267.

Jolliffe, I.T. (2002). *Principal Component Analysis*, 2nd ed. New York: Springer-Verlag.

López-Santos, M.C., Yubero, F., Espinós, J.P. & González-Elipe, A.R. (2010). Non-destructive depth compositional profiles by XPS peak-shape analysis. *Anal Bioanal Chem* **396**, 2757–2768.

Malinowski, E.R. & Howery, D.G. (1980). *Factor Analysis in Chemistry*. New York: Wiley.

Payne, B.P., Grosvenor, A.P., Biesinger, M.C., Kobe, B.A. & McIntyre, N.S. (2007). Structure and growth of oxides on polycrystalline nickel surfaces. *Surf Interface Anal* **39**, 582–592.

Savitzky, A. & Golay, M.J.E. (1964). Smoothing and differentiation of data by simplified least squares procedures. *Anal Chem* **36**, 1627–1639.

Smith, E.F., Briggs, D. & Fairley, N. (2006). Further developments in quantitative X-ray photoelectron spectromicroscopy: Preliminary results from the study of germanium corrosion. *Surf Interface Anal* **38**, 69–75.

Tanuma, S., Powell, C.J. & Penn, D.R. (1994). Calculations of electron inelastic mean free paths. V. Data for 14 organic compounds over the 50–2000 eV range. *Surf Interface Anal* **21**, 165–176.

Tougaard, S. (1987). X-ray photoelectron spectroscopy peak shape analysis for the extraction of in-depth composition information. *J Vac Sci Technol A* **5**, 1275–1278.

Tougaard, S. (1990*a*). Formalism for quantitative surface analysis by electron spectroscopy. *J Vac Sci Technol A* **8**, 2197–2203.

Tougaard, S. (1990*b*). Inelastic background correction and quantitative surface analysis. *J Electron Spectrosc Relat Phenom* **52**, 243–271.

Tougaard, S. (1996). Surface nanostructure determination by X-ray photoemission spectroscopy peak shape analysis. *J Vac Sci Technol A* **14**, 1415–1423.

Tougaard, S. (1997). Universality classes of inelastic electron scattering cross-section. *Surf Interface Anal* **15**, 137–154.

Tougaard, S. (1998). Accuracy of the non-destructive surface nanostructure quantification technique based on analysis of the XPS or AES peak shape. *Surf Interface Anal* **26**, 249–269.

Tougaard, S. (2003). Quantitative X-ray photoelectron spectroscopy: Simple algorithm to determine the amount of atoms in the outermost few nanometers. *J Vac Sci Technol A* **21**, 1081–1086.

Tougaard, S. (2005). Algorithm for automatic X-ray photoelectron spectroscopy data processing and X-ray photoelectron spectroscopy imaging. *J Vac Sci Technol A* **23**(4), 741–745.

Tougaard, S. (2013). Validity of automated X-ray photoelectron spectroscopy algorithm to determine the amount of substance and the depth distribution of atoms. *J Vac Sci Technol A* **31**, 031502-1–6.

Tougaard, S. & Hansen, H.S. (1989). Non-destructive depth profiling through quantitative analysis of surface electron spectra. *Surf Interface Anal* **14**, 730–738.

Walton, J. & Fairley, N. (2005). Noise reduction in X-ray photoelectron spectromicroscopy by a singular value decomposition sorting procedure. *J Electron Spectrosc Relat Phenom* **148**, 29–40.

Walton, J. & Fairley, N. (2006). Characterisation of the Kratos Axis Ultra with spherical mirror analyser for XPS imaging. *Surf Interface Anal* **38**, 1230–1235.